

Spin Cooperated Catalytic Activities in Mn-N₄ based Single-atom Nanozyme: Mechanisms and a Brief Charge-spin Model

Ling Liu^{1,†}, Shaofang Zhang^{1,†}, Xinzhu Chen^{1,†}, Guo Li², Yonghui Li^{2*}, Xiao-Dong Zhang^{1,2*}

1. Tianjin Key Laboratory of Brain Science and Neural Engineering, Academy of Medical Engineering and Translational Medicine, Tianjin University, Tianjin 300072, China

2. Department of Physics and Tianjin Key Laboratory of Low Dimensional Materials Physics and Preparing Technology, School of Sciences, Tianjin University, Tianjin 300350, China

3.

* yonghui.li@tju.edu.cn

* xiaodongzhang@tju.edu.cn

†: These authors have contributed equally.

ABSTRACT

Although developing artificial enzymes has made great progress, there is still a gap between artificial enzymes and natural enzymes in catalytic performance. Designing and constructing efficient artificial biocatalysts is extremely desirable because of their high stability, low cost and easy storage. Here, we report a synthesized amino-functionalized graphene quantum dots-based manganese single atom catalyst (SAC) Mn-N₄, which exhibits POD-, CAT, SOD-like activities, especially the superior SOD-like activity. Recent studies have reported Mn-based SAzymes, however, the multi-enzyme mimicking catalytic mechanisms for Mn-N₄ are not comprehensive and in-depth enough. Therefore, we combine density functional theory (DFT) calculations and machine learning (ML) to validate the performance of the multi-enzyme mimicking activities. The DFT simulations show that Mn-N₄ owns a highly effective SOD in the “one-side adsorption” with a very low energy barrier of 0.077 eV, which can be attributed to variation of the preferred spin states of Mn-O₂^{•-} system and its “spin flip-collection lock” in the SOD-like catalytic procedure. Furthermore, spin related charge distributions on Mn-N₄ configurations by machine learning (ML) analysis suggest that the pattern of spin and natural charge/valence electron distribution will exhibit similarity in the structures of multiple intermediate steps of multi-enzyme mimicking activities. This work not only puts forward the catalytic mechanisms of Mn-N₄ SAzymes, but also provides essential guidance for future design of highly performance artificial enzymes.

1. Introduction

Nanozyme engineering, as an interdisciplinary of chemistry, biology and physics, aim to development of artificial enzymes for precise transformations¹. Compare with natural enzymes, many nanozymes show superior biocatalytic activities and selectivity which can be modified by molecular engineering. From the perspective of designing new catalytic materials, building a heterogeneous structure are usually a successful strategy to trigger quantum mechanical effect of materials. In a work back to 1999, surface metal atoms modified heterogeneous catalyst, Pt cations on MgO is reported². Since the peroxidase-like activity of Fe₃O₄ nanoparticles was first reported in 2007³, a variety of nanozymes, including metals, metal oxides, and carbon nanomaterials have been studied as enzyme mimics due to their high stability, low cost, easy storage and multifunctionalities. After some earlier development, researchers narrow the activation sites to a single one⁴ which eventually lead the emergence of M-N-C structure (a.k.a. M-N_x structures) for potential nanozyme applications in electrocatalysis⁵, organic transformation⁶, photocatalysis⁷ and biocatalysis⁸.

Earlier investigations in M-N_x family focus on Fe-N₄ and Mn-N₄⁹ and they show pronouncing enzyme-like behaviors. Fe-N_x structure is fabricated into nanotubes and being tested for its peroxidase-mimicking activity¹⁰. Other reports with different metal acts as the central catalytic site are reported. Xu et al. synthesized a Zn-N₄ structure as antioxidant nanozyme and apply it to wound disinfection applications¹¹. In 2019, Co-N₅, Fe-N₅ and Mn-N₅ as a new series of single-atom nanozyme are added to the M-N_x family¹². After Chen et. al. synthesized the M-N₄ (M=Cr, Mn, Fe, Co, Cu) materials¹³, Zhang et. al. extend the M-N_x family by introducing a FeCu-N₆ structure¹⁴. These new materials set up a new space for researchers to explore and adjust for new nanozymes.

Based on the structure of M-N_x family of materials as nanozymes, the catalytic mechanisms are explored with theoretical tools. Nanozyme show enzyme-like reactions as oxidase, catalase, peroxidase, superoxide dismutase, glutathione peroxidase and more. Simulations focus on the binding and separation between nanozymes and superoxide/hydroxyl radical/oxygen atoms/hydrogen peroxide/etc^{11,14-18}. However, the Mn-N₄ catalyzed reaction mechanism is still unclear. Due to the magnetic properties of Mn, its spin seems to play an important role in the reactions. So, in this work, we explore the nanozyme behaviors of Mn-N₄ including catalase-like, peroxidase-like, superoxide dismutase-like behaviors with spin involved critical structures. A brief data-oriented model is also provided to draw the connection between electron distribution and spin change.

On the other hand, previous studies have been devoted to exploring the relationship between spin states and catalytic activity of catalysts containing metal active sites. Lubomír Rulíšek et. al. studied the detailed reaction mechanism of iron and manganese superoxide dismutase with density functional calculations on realistic active-site models and proposed that the reaction mechanisms and spin states seem to have been designed to avoid spin conversions or to facilitate them by employing nearly degenerate spin states¹⁹. Martin Srncic et.al. studied reaction mechanism of manganese superoxide dismutase using QM/MM approach at the density functional theory level and suggested that the oxidation of O₂⁻ to O₂ most likely occurs by an associative mechanism following a two-state (quartet-octet) reaction profile²⁰. However, the previous researches on the relationship between spin and catalysis are not deep enough, and most of the works are limited to reaction mechanism of SOD.

In this work, inspired by the synthesized of single atom catalyst Mn-N₄ in experiment, the structures, multi-enzyme mimicking catalytic activities of Mn-N₄ are explored by both experimental methods and theoretical calculations. By doping Mn single atom into the amino-functionalized graphene quantum dots, Mn-N₄ displays outstanding SOD-like activities. To understand the origin of the specific efficient SOD-like activities, the possible reaction mechanisms (“one-side adsorption” and “bilateral adsorption”) of POD-like, CAT-like and SOD-like activities are systematically investigated by density functional theory (DFT) simulations. The simulation results reveal that Mn-N₄ can smoothly activate two O₂⁻ to form H₂O₂ and O₂ molecules in succession in the “one-side adsorption” of SOD-like reaction, which can be attributed to variation of the preferred spin states of Mn-O₂⁻ system and its “spin flip-collection lock” in the SOD-like catalytic procedure. Last but not least, spin related charge distributions on Mn-N₄ configurations by machine learning (ML) analysis suggest that the pattern of spin and natural charge/valence electron distribution will exhibit similarity in the structures of multiple intermediate steps of multi-enzyme mimicking activities. This work for the first time correlates the spin with multi-enzyme mimicking activities of Mn-N₄ and will provide essential

guidance for the future design and synthesis of highly active enzyme mimics and help understand the rational catalytic mechanisms of nanozymes.

2. Experimental results and theoretical methods

Preparation of Mn single-atom nanozymes

The Mn single-atom nanozymes were synthesized by a two-step method. First, the amino-functionalized graphene quantum dots were prepared using a hydrothermal method. The procedures were as follows: 2 g of pyrene was nitrated in 160 mL of concentrated nitric acid by condensing and refluxing in an oil bath at 80 °C for 13 h. After the reaction solution was cooled to room temperature, it was washed several times by deionized water and then dried under vacuum to obtain neutral trinitropyrene. After that, 300 mg of trinitropyrene, 55 mL of deionized water and 5 mL of concentrated ammonia were added sequentially into a centrifuge tube, and the mixture was crushed in an ice water bath using a cell crusher for 2 h. The mixture was transferred to a stainless steel reactor lined with polytetrafluoroethylene and kept at 180 °C for 10 h. The larger and smaller products as well as the unreacted reagents were removed by centrifugation and dialysis to collect the final amino-functionalized graphene quantum dots. In the second step, the Mn atoms were anchored to the graphene quantum dots. The 0.01 mmol of MnCl₂ was dissolved in 30 mL of amino-functionalized graphene quantum dots, and the mixture was sonicated for 15 min and then freeze-dried to obtain the powder. The obtained powder was mixed with urea at a mass ratio of 1:10 and ground evenly. The mixed powder was transferred to a tube furnace and activated at 500 °C for 2 h under Ar atmosphere to obtain Mn single-atom nanozymes.

Structural characterization of Mn single-atom nanozymes

The atomic information and element distribution of single-atom nanomases were observed by the spherical aberration-corrected atomic resolution microscope (JEM-ARM200F, JEOL, Japan) and field-emission transmission electron microscopes (JEM-2100F, JEOL, Japan), operating at an accelerating voltage of 200 kV. X-ray diffractometer (XRD, Smartlab, Japan) equipped with Cu K α radiation was used to detect the structure of the Mn single-atom nanozymes in the range of 10°-60°. The Al K α -excited X-ray photoelectron spectroscopy (XPS, Axis Supra, Kratos) was employed to analyze the element composition and bonding information of Mn single-atom nanozymes. Raman spectrometer (DXR Microscope, Thermo Electron Corporation, USA) equipped with a 532 nm He-Ne laser was used to measure the structure of Mn single-atom nanozymes under a scanning wavenumber range of 800 to 3000 cm⁻¹.

Enzyme-mimic activity measurements:

The POD-like activity of Mn single-atom nanozymes was tested using the TMB substrate chromogenic kit (TELISA, SenBeiJia). According to the instructions, the TMB chromogenic solution, TMB buffer solution and TMB oxidant were mixed into a working solution at a volume ratio of 5000:5000:4. Then 20 μ L of MnN₄ at different concentrations (10, 20, 40, 60, 80 and 100 μ g/mL) and 180 μ L of working solution were mixed as the experimental group, 20 μ L of the graphene carriers without Mn atom loading instead of nanozymes as the experimental control group, 20 μ L of deionized water instead of nanozymes as the blank control group. The reaction mixture were added into a 96-well plate, the absorbance values at 652 nm were measured in real time using a microplate spectrophotometer (SuPerMax 3000FA, Shanghai Flash Spectrum). Finally, the catalytic rate for the first 5 min of the reaction was calculated.

Since natural catalase can catalyze the decomposition of H₂O₂ to H₂O and O₂, the CAT-like activity of Mn single-atom nanozymes was assessed by using UV-visible spectrophotometer to detect the change of H₂O₂ content in the reaction system containing nanozymes. The 30 μ L of Mn single-atom nanozymes (500 μ g/mL) was mixed with 270 μ L of H₂O₂ (40 mmol/L), and the change of absorbance in the reaction system after the addition of the nanozymes was immediately detected at 240 nm using a UV-Vis spectrophotometer. After 120 minutes of

reaction, the H₂O₂ scavenging rate of nanozymes was determined by the equation: clearance rate = (A_{0 min} - A_{120 min})/A_{0 min}*100%. Finally, the decomposition rate of H₂O₂ by nanozymes was calculated for the first 20 min of reaction.

The SOD-like activity of the nanozymes was assayed using the Total Superoxide Dismutase Assay Kit with NBT (R22261, Yuanye). Firstly, the SOD buffer, NBT colorimetric solution and enzyme solution were mixed in the ratio of 100:30:30 to form the SOD working solution. In the assay, 160 μL of working solution, 20 μL of nanozymes at different concentrations (100, 200, 300, 400 and 500 μg/mL), 20 μL of reaction starter solution were added into the 96-well plate, respectively. The nanozymes were replaced by SOD buffer as the lighting control group, and 96-well plate was irradiated under lamp for 10 min until the lighting control group turned blue-green. The light-avoiding control group was incubated in the dark for the same time with 20 μL of SOD buffer instead of the nanozymes. Then, the absorbance at 560 nm (A₅₆₀) of each group was recorded by a microplate spectrophotometer and the absorption spectra at 300-800 nm were detected by a UV-vis spectrophotometer. The inhibition rate of nanozyme on formazan was calculated according to the formula: inhibition rate (%) = (A_{lighting} - A_{nanozymes})/(A_{lighting} - A_{light-avoiding}) × 100%. The inhibition rate of nanozyme on formazan was calculated according to the formula: The values of SOD-like activity were determined by the formula: activity (Unit) = inhibition rate/(1 - inhibition rate).

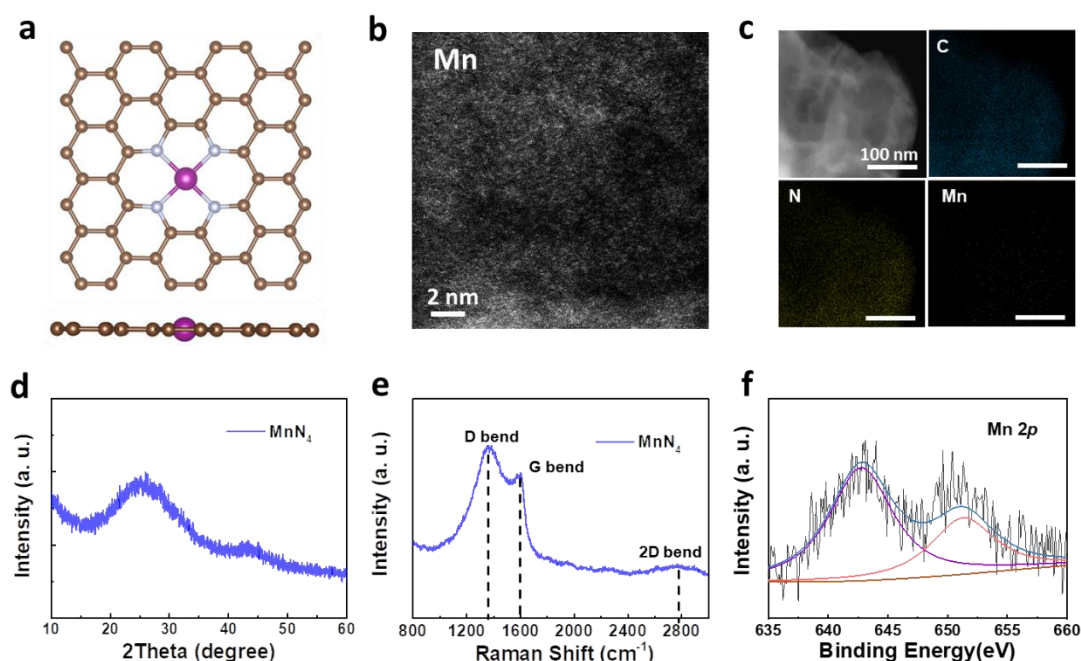


Figure 1 The structural characterization of Mn single-atom. (a) The optimized structures of MnN₄. (b) The AC-HAADF-STEM and (c) EDS mapping images of Mn single-atom nanozymes. The (d) XRD and (e) Raman spectra of Mn single-atom nanozymes. (f) XPS spectra of Mn single-atom nanozymes in Mn 2p region.

Since Mn-N₄ showed POD, CAT, and SOD-mimicking activities, mechanisms for POD-like, CAT-like, and SOD-like activities of Mn-N₄ catalyst are as important as the electron structure analysis of the catalyst. Therefore, two models are designed and simulated. Considering the structure of the substrate material, the first model (for catalytic energy profile simulations) is constructed as a graphene flake with its central region replaced by a single metal atom and four N atoms surrounded. The second model (for analysis of the electron structure of the catalyst) is constructed as a 12.78Å×12.30Å supercell with a Mn-N₄ embedded graphene sheet. To avoid the interaction between layers due to periodicity and improve the reliability and accuracy of calculations, a 15 Å vacuum distance is taken along the z-direction perpendicular to the surface of catalysts.

With the first model, intermediate states can be obtained by fully relaxing geometries of the flake with fragments/reactants attached. Intermediate and transition states are minima and saddle points on the energy surfaces along the reaction coordinates. Based on modeled structures, all the intermediate and transition states

in multi-enzyme catalytic reactions are simulated by Density Functional Theory (DFT) using the Gaussian 09 package (cite). The 6-31G(d,p) basis set is used as a balanced approach between computational workload and accuracy. DFT approximated the electron-electron interactions as a background functional of electronic density, and the functional is generally split into 2 parts, the Hartree potential and the exchange-correlation potential. The well-known B3LYP is chosen as the exchange-correlation potential. All structures are calculated at all possible spin (up to 10 in spin multiplicity) states in this work. All structures are confirmed by frequency calculations such that each intermediate state do not show any imaginary frequencies at its minimum energy and each transition state shows only one imaginary frequency. The corresponding zero-point-energy (ZPE) and thermal corrections of frequency analyses were performed at the same level of theory to obtain Gibbs free energies.

To evaluate other properties such as the stability and electronic properties of Mn-N₄ catalyst, the formation energies, charge density difference, electron localization function (ELF), and density of states (DOS) are investigated with the Vienna ab initio Simulation Package (VASP)^{21,22}. The elemental core and valence electrons are represented using the projector augmented wave (PAW) method^{23,24}. The Perdew–Burke–Ernzerhof generalized gradient approximation (GGA-PBE) functional²⁵ is employed to estimate the exchange–correlation potential energy. The convergence of calculations is ensured by setting the cutoff energy for the plane-wave basis at 500 eV. In addition, Brillouin zone integrations are performed according to the Monkhorst-Pack scheme⁵ using a 4 × 4 × 1 k-mesh. In structural relaxations, the convergence criteria for energy and force are set to 1 × 10⁻⁶ eV and -0.01 eV/Å, respectively. The van der Waals (vdW) interaction is considered by allowing the D3 correction^{26,27} and the spin polarizations are considered in all calculations. The formation energies (E_f) of structures are calculated by equation 1.

$$E_f = E_{total} - n_C E_C - n_N E_N - n_{Mn} E_{Mn} \quad (1)$$

Where E_{total} represents the total energy of the N₄-G/Mn-N₄ configuration, E_C , E_N and E_{Mn} represent the energy of a carbon atom in graphene, half of a N₂ molecule energy in the gas phase, and the energy per atom for Mn, respectively. n_C , n_N and n_{Mn} are the total numbers of C, N and Mn atoms, respectively.

3. The structures and charge distributions of Mn-N₄

High-density Mn single-atom nanozyme were prepared using amino-functionalized graphene quantum dots as the substrate, and their geometric structures are displayed in Figure 1a²⁸. The individual Mn atoms of the MnN₄ were observed by aberration-corrected high-angle annular dark-field scanning transmission electron microscopic (AC-HAADF-STEM) (Figure 1b), with bright dots representing Mn atoms marked by yellow circles. The corresponding energy-dispersive X-ray spectroscopy (EDS) mapping showed that Mn, C and N are uniformly distributed in the MnN₄ (Figure 1c). The X-ray diffraction (XRD) spectrum exhibited two broad characteristic peaks near 25° and 44°, which correspond to the (002) and (010) lattice planes of graphitic C, respectively, and there were no atomic aggregation states and metal oxides (Figure 1d). Similarly, the D-band peaks at 1328 cm⁻¹ and 2700 cm⁻¹ in the Raman spectrum indicated typical N-doped graphene (Figure 1e). Further, the element species and valence analysis of the MnN₄ were determined by X-ray photoelectron spectroscopy (XPS). The C species were divided into C=C, C-N and O-C=O bonds, and N phase consisted mainly of pyrrole N, pyridine N and graphitic N (Figure S1). The Mn 2p region was located at 642.8 and 651.3 eV, which were attributed to Mn²⁺ 2p_{3/2} and Mn²⁺ 2p_{1/2}, respectively (Figure 1f).

To evaluate the structural stability of Mn-N₄ configuration, the electron structure level of comparisons between N₄-G and Mn-N₄ are provided including formation energies, charge redistributions, bonding properties and density of states. As calculated according to equation (1), (shown in Figure 2a), E_f of the N₄-G structure is 1.709 eV. After the incorporation of Mn atom, the reduction of E_f to -1.139 eV demonstrates that Mn-N₄ is energetically favored. The optimized geometries shows that all atoms in both N₄-G and Mn-N₄ structures are kept nearly in the same plane as shown in Figure 1a. Next, the charge density differences of these two models are simulated (Figure 2a and 2d). N₄-G in Figure 2a shows that the charges are uniformly distributed around N atoms due to the symmetry of the N₄ pattern. After introducing the Mn atom to the center, remarkable charge rearrangement occurs, and the Mn atom tends to lose electrons to the surrounding N atoms (Figure 2d) while carbon atoms on the graphene also donate electrons to N atoms. The electron distributions in the N₄-G and Mn-

N_4 configurations are further verified by the ELF images (Figure 2b and 2e). As shown in Figure 2b, unpaired (represented by green) and lone pair (represented by orange) electrons around every N atom extend towards the center in N_4 -G. With the incorporation of the Mn atom, the unpaired electrons as well as the lone pair electrons of the N atoms contribute to Mn-N interactions, thus electrons around Mn behave like free electrons, which is displayed in the ELF image of Figure 2e. Besides, the electronic structures of N_4 -G and Mn- N_4 are also examined by DOS analysis (Figure 2c and 2f), based on the DOS plot in Figure 2c, the electronic states are almost equally filled both in spin-up and spin-down. While the DOS pattern (Figure 2f) is markedly altered after the incorporation of the Mn atom, which eliminates the band gap of N_4 -G and is expected to decrease the energy barrier for species' adsorption²⁹.

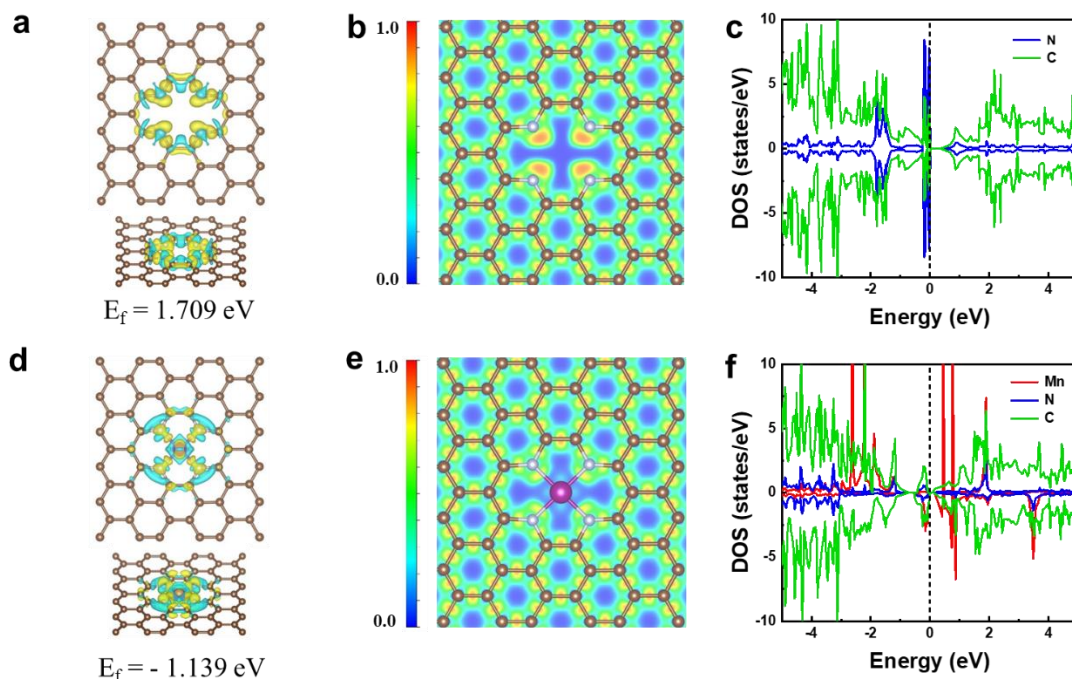


Figure 2 Top view of the charge density difference of (a) N_4 -G and (d) MnN_4 with the isosurface of $0.005 \text{ e} \text{ \AA}^{-3}$. cyan and yellow areas represent charge density depletion and accumulation, respectively. ELF images of (b) N_4 -G and (e) MnN_4 . The density of states (DOS) of (c) N_4 -G and (f) MnN_4 .

4. Mechanisms for enzyme-mimicking catalytic reaction

To reveal the Mn- N_4 multi-enzyme like activities including the POD-like, SOD-like and CAT-like performances, comprehensive DFT simulations are carried out. The structures with the lowest energy of all of the intermediate states (INT) and transition states (TS) involved in the POD-, CAT-, and SOD-like reaction activities are shown with the energy profiles in Figure 3-6 and Figure S2-5. Structures with heavy spin contamination are discarded in this work.

4.1 Mechanisms for POD-like catalytic activities of Mn- N_4 .

The POD-like catalytic process is a process that decomposes H_2O_2 into H_2O . To investigate the catalytic performance of the MnN_4 in enzyme-mimic catalysis, the POD- mimic reaction is first detected using colorimetric method. Compared to the graphene carriers without Mn atom loading (N/C), the MnN_4 dramatically catalyzes the substrate TMB within 60 min, confirming that the excellent POD-like activity originates from the introduction of single-atom Mn (Figure 3a). The concentration-dependent catalytic rate is quantified for MnN_4 , which is as high as $3.31 \mu\text{M}/\text{min}$ at $10 \mu\text{g}/\text{mL}$ (Figure 3b). In addition, ESR tests reveal the significant hydroxyl radicals ($\bullet\text{OH}$) scavenging ability of MnN_4 (Figure 3c).

The POD-like catalytic mechanism of Mn- N_4 is investigated based on a variety of intermediate/transition states of Mn- N_4 catalyst attached to different chemical groups. The POD-like activity which can be evaluated by the 3,3',5,5'-tetramethylbenzidine (TMB) colorimetric method, is simplified in our simulation by replacing TMB by hydrogen atoms. Simulation results of different reaction pathways suggest that Mn- N_4 prefers the

“bilateral adsorption” process of activating H_2O_2 by forming the Mn-O- N_4 structure with an active center through the heterolytic path as shown in Figure 3. The “bilateral adsorption”, according to previous works^{14,16}, is primarily attributed to the unique “two-sided oxygen-linked” catalytic reaction path which explain the high catalytic activity of MN_x due to the increase the utilization of catalyts.

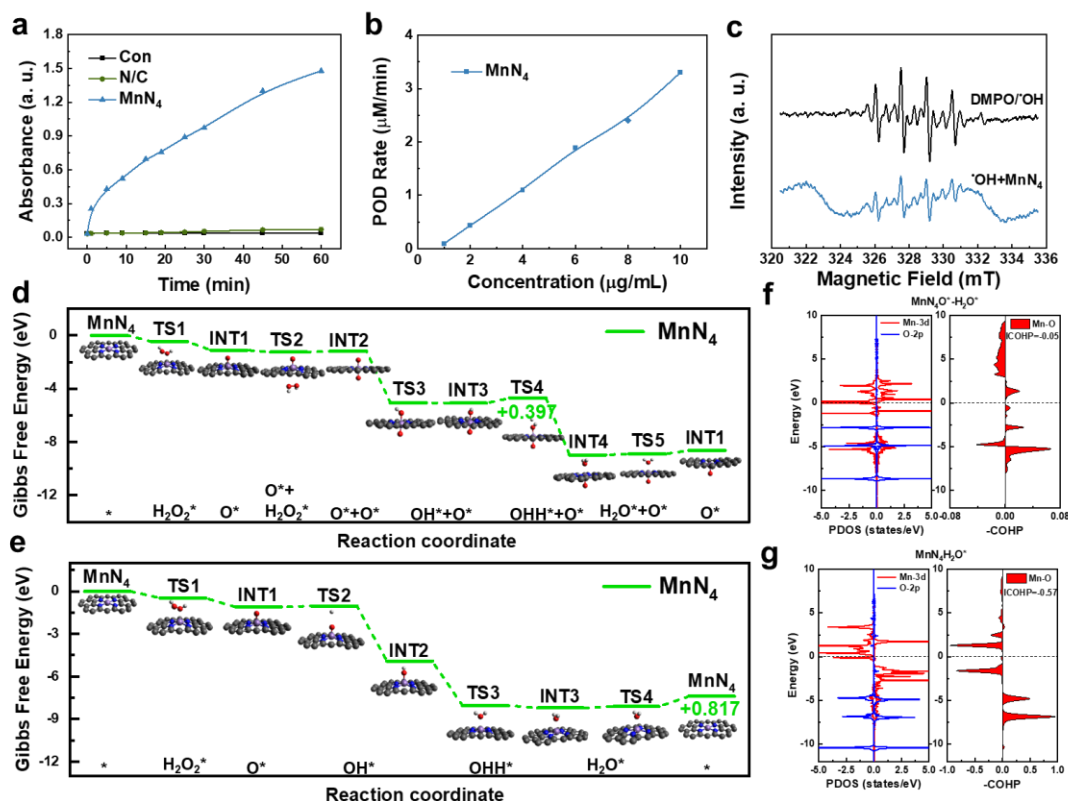


Figure 3 POD-mimic activity of Mn single-atom nanozymes. (a) Reaction-time curves of the POD-mimic reaction with TMB as substrate catalyzed by Mn single-atom nanozymes at 10 $\mu\text{g/mL}$. (b) Concentration-dependent reaction rate of Mn single-atom nanozymes catalyzing TMB within 5 minutes. (c) The $\bullet\text{OH}$ scavenging ability of Mn single-atom nanozymes. Calculated reaction energy profiles corresponding to the peroxidase-like activity for the heterolysis of H_2O_2^* of MnN_4 corresponding to (d) bilateral mechanism and (e) one-side adsorption mechanism. The purple, blue, gray, red, and white balls represent the Mn, N, C, O, and H atoms, respectively. The DOS and COHP of (f) $\text{MnN}_4\text{O-H}_2\text{O}^*$ and (g) $\text{MnN}_4\text{-H}_2\text{O}^*$. All 2p orbitals indicate the O 2p orbitals in H_2O^* and all COHP is calculated for the Mn-O interaction, O indicates the oxygen atom in H_2O^* .

The “bilateral adsorption” mechanism in the catalytic process shows a remarkably low activation energy which should be extensively discussed along the reaction pathway. As shown in Figure 3d and Figure S2a, the reaction pathway roughly goes through four steps: H_2O_2 molecule activation (step i), bilateral adsorptions (step ii), hydrogen attractions (step iii), H_2O molecule desorption (step iv). (i) First, a H_2O_2 molecule can be activated by absorbing on the Mn- N_4 site. (ii) Then the H_2O_2 can be dissociated by generating a O^* intermediate (INT1 in Figure 3d and S1a) and a water molecule. And another H_2O_2 molecule can be captured by the vacant side of the active site and forms an O^*+O^* intermediate state (INT2 of Figure 3d and Figure S2a) with a very small barrier of 0.072 eV. (iii) Subsequently, an O^* on active site attracts two hydrogen atoms successively to form O^*+OHH^* intermediate state (INT4 of Figure 3d and Figure S2a), yielding one H_2O molecule, which is easily surmountable for Mn- N_4 , and this step is the rate-determining step (RDS) with a small barrier of 0.397 eV. (iv) Finally, this molecule desorbs from the catalyst with a low barrier of 0.334 eV, which is smaller than the RDS.

As shall be demonstrated, the “bilateral adsorption” mechanism bypasses the release of the last H_2O molecule which corresponds to a 0.817 eV barrier which is the critical feature of reducing the activation energy along the reaction pathway. In contrast, the 0.817 eV barrier cannot be avoided in the “one-side adsorption” pathway. As shown in Figure 3e, after the formation of O^* intermediate, the O^* on the Mn active site can easily capture two H atoms consecutively to form OHH^* (INT3 of Figure 3e). To complete the catalytic procedure, the Mn- N_4 must return to its initial state by releasing a H_2O molecule. Therefore, the H_2O desorption is the RDS with energy barrier of 0.817 eV in “one-side adsorption”. If the “bilateral adsorption” behaved similarly by

releasing the last H₂O molecule (Figure S2a), such reaction pathway had no advantage in reaction rate based preference.

Moreover, to support the “bilateral adsorption” mechanism, the crystal orbital Hamilton population (COHP)³⁰ analysis is applied to investigate the bonding and antibonding contribution of the adsorbed groups and bonded Mn sites. To gain more insights into origins of higher POD-like activity (lower energy barrier) in the “bilateral adsorption”, the structures corresponding to the last H₂O molecule desorption (TS5 of Figure 3d and TS4 of Figure 3e) are studied. The COHP curves of Mn-O bond (between the Mn atom and the oxygen atom in H₂O) in MnN₄O-H₂O* and MnN₄-H₂O* are shown in Figure 3f and 3g, respectively. The integrated COHP (iCOHP) offers a quantitative evaluation of the bond strength in each moiety. The weakened Mn-O interaction is verified by a less negative iCOHP value in MnN₄O-H₂O* (-0.05 eV vs -0.57 eV in MnN₄-H₂O*) due to the extra O* on the other side. As shown by the DOS plot in Figure 3g, for MnN₄-H₂O*, strong p-d electronic states overlap in the low energy level (-6.9 ~ -4.9 eV) makes the bonding contributions (left panel of the COHP plot in Figure 3g) increase. While for MnN₄O-H₂O* in the DOS plot in Figure 3f, low-level electronic states (-4.7 eV) overlap by Mn 3d orbitals and O 2p orbitals makes the antibonding orbitals occupied, so more electrons are filled in the antibonding orbitals (left panel of the COHP plot in Figure 3f) far below the fermi level (-4.7 eV) for MnN₄O-H₂O* and thus the Mn-O is weakened.

Besides the •OH-producing catalytic reaction pathways are still simulated since such reaction pathway is found in similar materials based on some previous studies^{11,17,18}. Namely, the homolysis of H₂O₂ is also studied with “one-side adsorption” and “bilateral adsorption” catalytic processes adopted. As shown in Figure S3a, the energy barrier of the last H₂O desorption (RDS) is still 0.817 eV as the POD-like process above. And for “bilateral adsorption” catalytic process in Figure S3b, the homolysis of H₂O₂* to 2OH* on the other side of the Mn-N₄ catalyst is the RDS with an energy barrier of 1.244 eV. As a result, the homolysis of H₂O₂ is not energetically preferred among the reaction pathways.

4.2 Mechanisms for CAT-like catalytic activities of Mn-N₄.

In a CAT-like catalytic process, H₂O₂ is decomposed to O₂ and H₂O. The catalase (CAT)-mimic activity is assessed via monitoring the process of H₂O₂ decomposition catalyzed by the MnN₄. As shown in Figure 4a, the MnN₄ presents a higher catalytic efficiency of decomposition of H₂O₂ than that of the N/C. At 120 min, the H₂O₂ clearance rate of MnN₄ reaches 52.4%, 17-fold higher than that of N/C (Figure 4b). Figure 4c reveals a concentration-dependent catalytic rate with 210.7 μM/min at 50 μg/mL.

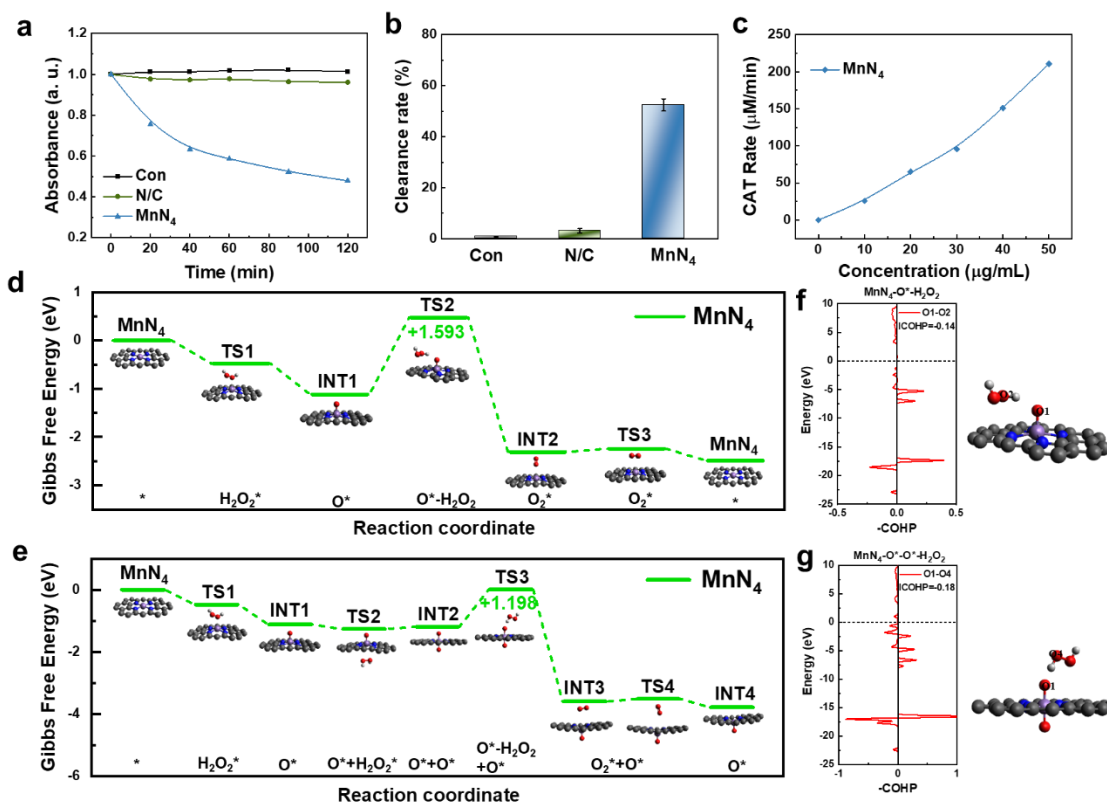


Figure 4 CAT-mimic activity of Mn single-atom nanozymes. (a) Reaction-time curves of H_2O_2 decomposition catalyzed by Mn single-atom nanozymes at $50 \mu\text{g/mL}$. (b) H_2O_2 clearance rates of Mn single-atom nanozymes at $50 \mu\text{g/mL}$. (c) Concentration-dependent H_2O_2 decomposition rate for the first 20 min. Calculated reaction energy profiles corresponding to the catalase-like activity of MnN_4 corresponding to (d) one-side adsorption mechanism and (e) bilateral adsorption mechanism. The purple, blue, gray, red, and white balls represent the Mn, N, C, O, and H atoms, respectively. The COHP of (f) $\text{MnN}_4\text{O}^*\text{-H}_2\text{O}_2$ and (g) $\text{MnN}_4\text{O}^*\text{-O}^*\text{-H}_2\text{O}_2$. All COHP is calculated for the O-O interaction, one O indicates the oxygen atom in H_2O_2^* , the other O indicates the oxygen atom on Mn.

The negligible CAT-like activity of Mn- N_4 can be attributed to the poor capacity for O^* moieties on the Mn sites to activate the approaching H_2O_2 molecules (INT1 of Figure 4d, INT2 of Figure 4e) in both the “one-side adsorption” and “bilateral adsorption” reaction pathways. In both reaction mechanisms, the transition from H_2O_2 molecule adsorption to the O^* intermediate state (INT1 of Figure 4d, INT2 of Figure 4e) in the CAT-like process is similar to that in POD-like process with the heterolysis of H_2O_2^* . So, it is important to focus on the RDS steps. In the “one-side adsorption” catalytic cycle, without extra hydrogens to react with, a high energy barrier of 1.593 eV, which is also the RDS, prevents the second H_2O_2 molecule from approaching to the O species on the Mn site easily. Then an oxygen atom is extracted from the H_2O_2 molecule to form the intermediate state O_2^* (INT2 of Figure 4d) and release one H_2O molecule. Although there is an O_2 detach from the Mn- N_4 surface, the energy barrier is as low as 0.066 eV.

In the “bilateral adsorption” reaction (Figure 4e and S4), the RDS has a 1.198 eV energy barrier (INT2 of Figure 5e and S4). With one O atom attached on each side, it is difficult for O^* on one side to attract the subsequent H_2O_2 molecule. Besides, after forming O_2^*+O^* intermediate (INT3 of Figure 5e and S4) and simultaneously generating a H_2O molecule, O_2 molecule desorbs from one side of the catalyst, which is a small energy uphill step (0.084 eV). Last, the restoration of the Mn atom is unlikely to happen, since its energy barrier is as high as 1.779 eV which means that the oxygen site in O^* (INT4 of Figure 4e and S4) can hardly obtain another oxygen in a H_2O_2 molecule to form O_2^* (INT5 of Figure S4). Even when the reaction process skip the restoration, the RDS is still as high as 1.198 eV.

To understand the origin of the poor CAT-like catalytic activity (higher energy barrier) of MnN_4 , the structures corresponding to the RDS (TS2 of Figure 4d and TS3 of Figure 4e) in “one-side adsorption” and “bilateral adsorption” are investigated. As shown in Figure 4f and 4g, the interaction between O^* (TS2 in Figure 4d, TS3 in Figure 4e) on Mn site and the O atom in an approaching H_2O_2 molecule is weak and can be validated by small value of iCOHP. And the small iCOHP values (-0.18 and -0.14 eV) indicate the difficulty in

H₂O₂ adsorption in both RDS steps. Therefore, the results of calculations suggest that the attracting for H₂O₂ molecule by the O* species on Mn site is almost unattainable either in “one-side adsorption” or “bilateral adsorption” mechanism of CAT-like catalytic activity.

4.3 Mechanisms for SOD-like catalytic activities of Mn-N₄.

In a SOD-like catalytic process, O₂^{•-} is decomposed to O₂ and H₂O. The quantification of superoxide dismutase (SOD)-mimic activity of the MnN₄ is performed based on nitro-blue tetrazolium (NBT) chromogenic principle. Figure 5a shows that the characteristic absorption of formazan disappears in the presence of MnN₄, indicating the superior SOD-like activity. The corresponding inhibition rate was as high as 81.2% at 50 μg/mL, much higher than 1.1% of N/C (Figure 5b). As shown in Figure 5c, the SOD-like value of MnN₄ is further determined to be 443 U/mg, 375 times higher than N/C.

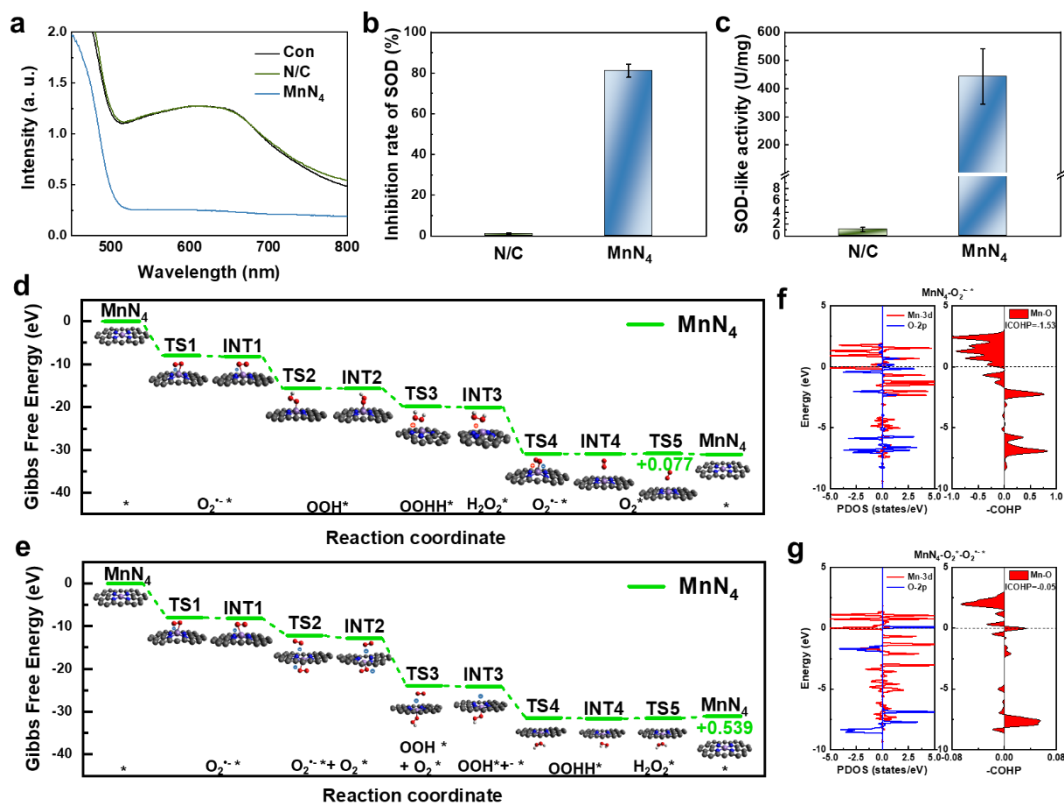


Figure 5 SOD-mimic activity of Mn single-atom nanozymes. (a) UV-vis absorption spectra of SOD-like activities with Mn single-atom nanozymes or N/C. (b) The corresponding inhibition rates of Mn single-atom nanozymes and N/C. (c) Quantification of SOD-like activity values of Mn single-atom nanozymes and N/C. Calculated reaction energy profiles corresponding to the superoxide dismutase-like activity of MnN₄ corresponding to (d) one-side adsorption mechanism and (e) bilateral adsorption mechanism. The purple, blue, gray, red, and white balls represent the Mn, N, C, O, and H atoms, respectively. The DOS and COHP of (f) MnN₄O₂^{•-}* and (g) MnN₄O₂^{•-}*-O₂^{•-}*. All 2p orbitals indicate the O 2p orbitals of one O atom in O₂^{•-}* and O₂^{•-}*, respectively and all COHP is calculated for the Mn-O interaction, O indicates the oxygen atom in O₂^{•-}* and O₂^{•-}*, respectively.

In contrast, the most efficient SOD-like abilities are dominated by “one-side adsorption” catalytic mechanisms in Mn-N₄ (Figure 5d). Due to the superoxide anion radical (O₂^{•-}) and proton (H⁺) species around the Mn site, the valences of the transition/intermediate states vary with the charge transfers in each step. Unlike the “bilateral adsorption” mechanism (Figure 5e), the “one-side adsorption” reaction pathway roughly goes through three steps: superoxide anion radical O₂^{•-} adsorption (step i), consecutive proton adsorptions and H₂O₂ molecule release (step ii), O₂ molecule generation and desorption (step iii). (i) First, the superoxide anion radical O₂^{•-} readily adsorbs on the surface to form O₂^{•-}* (INT1 in Figure 5d). The calculations suggest that adsorption of O₂^{•-} on the surface is highly exothermic process and is thus facile with no barriers. (ii) After two successive proton adsorptions, a H₂O₂ molecule generates (INT3 in Figure 5d) and the process is energetically and kinetically favorable in Gibbs free energy. (iii) With the desorption of the H₂O₂ molecule, another superoxide anion radical can be facily adsorbed on the catalyst to form an O₂^{•-}* transition state (TS4 in Figure 5d). Due to

the combination of the electron from the $O_2^{\cdot-}$ and an extra proton from the Mn-N₄ catalyst, an O₂ molecule forms (INT4 in Figure 5d) and then desorbs from the surface with a very low energy barrier of 0.077 eV, which is the RDS in the “one-side adsorption” mechanism. Finally, the Mn-N₄ recovers to its initial status.

On the other hand, the RDS in the “bilateral adsorption” catalytic mechanism is the restoration of Mn-N₄ (TS5 → Mn-N₄) with a 0.539 eV energy barrier. Though, in the proposed “bilateral adsorption” mechanism, an oxygen molecule is released before the release of an H₂O₂ molecule, the energy increase in the restoration step cannot be avoided. As shown in Figure 5f and 5g, the Mn-O interaction in the first adsorption of O₂^{•-} is weakened by the adsorption of the second O₂^{•-}. Such weakening can be represented by the iCOHP of Mn-O which is reduced from -1.53 eV (in Mn-N₄-O₂^{•-}) to -0.05 eV (in O₂^{•-}-Mn-N₄-O₂^{•-}). In addition, it can be seen from the DOS (Figure 5f and 5g) that d-p hybridization contributes less to bonding orbitals at deep levels for O₂^{•-}-Mn-N₄-O₂^{•-}. Therefore, the decreased Mn-O interaction is responsible for the converting from adsorbing O₂^{•-} to desorbing O₂ on one-side of the Mn-N₄ surface due to the extra O₂^{•-} on the other side.

4.4 “Spin flip-collection lock” in the SOD-like catalytic procedure

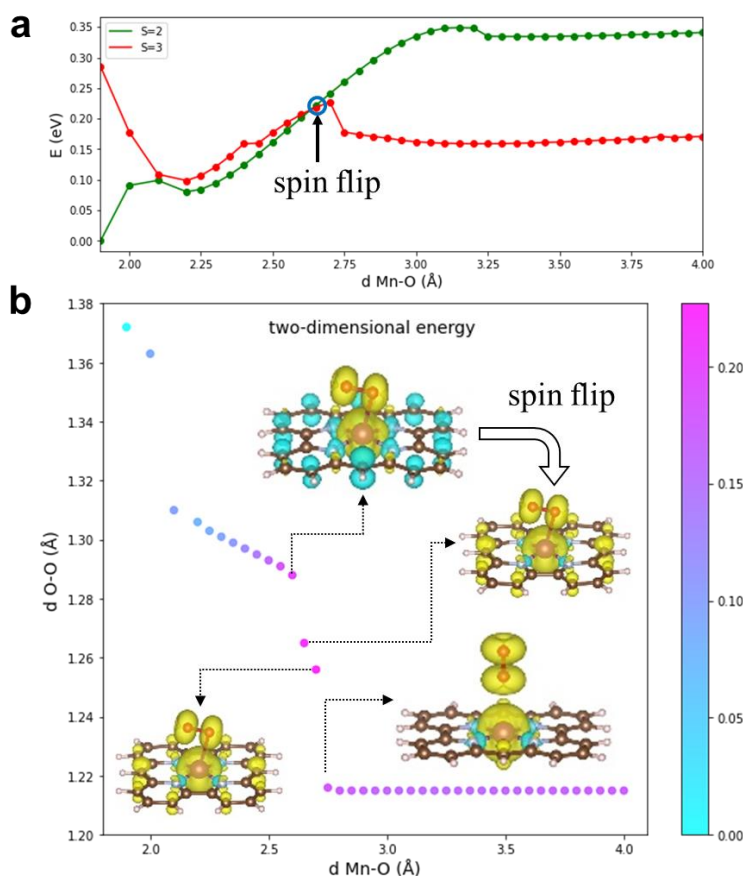


Figure 6 The energy profiles along with the Mn-O distances corresponding to the converting from superoxide anion radical $O_2^{\cdot-}$ to O₂ molecule on the active site of MnN₄ at two spin states ($S=2, 3$). Spin density of MnN₄-O₂^{•-} and MnN₄-O₂ are also plotted (yellow stands for spin up and cyan for spin down).

In a more detailed electron structure analysis, the mystery behind the adsorption of O₂^{•-} is close related to states of spin which are dynamically related to the small changes in the Mn-O distance. The attached O₂^{•-} cannot be released immediately in the form of an oxygen molecule. Such forbidden can be demonstrated as a “spin flip-collection lock” mechanism.

To demonstrate the critical moment of the “spin flip-collection lock”, a series of relaxed scans are performed based on the constrained optimization. In each step of the process of the scan, the Mn-O distance is fixed at a particular value and the other variables are relaxed. Initially, one oxygen atom in the superoxide anion O₂^{•-} is at a distance of 1.9 Å from the manganese, the Mn-O distance increases by 0.05 Å with each scanning step, eventually moving to a distance of 4 Å from each other. As shown in Figure 6 and Figure S5, the

simulated energy profiles along the process from adsorbing O_2^{*} to desorbing O_2^* defined by the Mn-O distance at different spin states are depicted.

As shown in Figure 6a, at a Mn-O distance of ~ 2.65 Å, “spin flip lock” unlocks, namely, from this crossing point on (Figure 6a), the spin state of the more energetically favorable structures then changes from quintet ($S=2$) to septet ($S=3$) state. The quintet-septet crossing is the energy uphill point on the profile with an activation barrier of about 0.218 eV with respect to the initial quintet state at 1.9 Å, suggesting that this “spin flip” needs to overcome an energy barrier. Moreover, as shown in Figure 6b, at a Mn-O distance of ~ 2.60 Å, the spin density shows that Mn and O_2^- on the site own the same spin direction, while the four coordinated N atoms and some neighboring C atoms on the catalyst surface display the opposite spin of Mn and O_2^- . When the “spin-flip” occurs at a Mn-O distance of ~ 2.65 Å, the spin direction of these C atoms on the catalyst flips to the same as Mn and O_2^- moiety. When the Mn-O distance is elongated to 2.70 Å, the spin direction of all the atoms on Mn-N₄ catalyst almost keeps unchanged, and as the Mn-O distance continues to elongate to 2.75 Å, an O_2 molecule generates and collects the spin densities from catalyst. In addition, the “spin flip” also brings changes in O-O bond length in O_2^- moiety. In Figure 6b, the O-O bond lengths of O_2^{*} moiety become shorter (from 1.372 to 1.288 Å) as the Mn-O distance increases from 1.90 to 2.60 Å, and the “spin flip” keeps locking. Then, the O-O distance of O_2^{*} moiety decreases to 1.265 Å when the “spin-flip” occurs. Subsequently, the energy rises to the highest at a Mn-O distance of ~ 2.70 Å, and the O-O bond length of O_2^{*} moiety decreases to 1.256 Å. After that, the O-O bond length dramatically reduces to 1.216 Å with the Mn-O distance increases to 2.75 Å, an O_2 molecule generates simultaneously and the energy dramatically drops after the highest point (0.227 eV) and then tends to flatten (Figure 6a). Therefore, the simulations indicate that the conversion from adsorbing O_2^{*} to O_2 desorption needs to overcome a small energy barrier of 0.227 eV due to the presence of this “lock”, as the step i of SOD-like reaction pathway described above.

4.4 Spin related charge distributions on Mn-N₄ configurations by machine learning (ML) analysis.

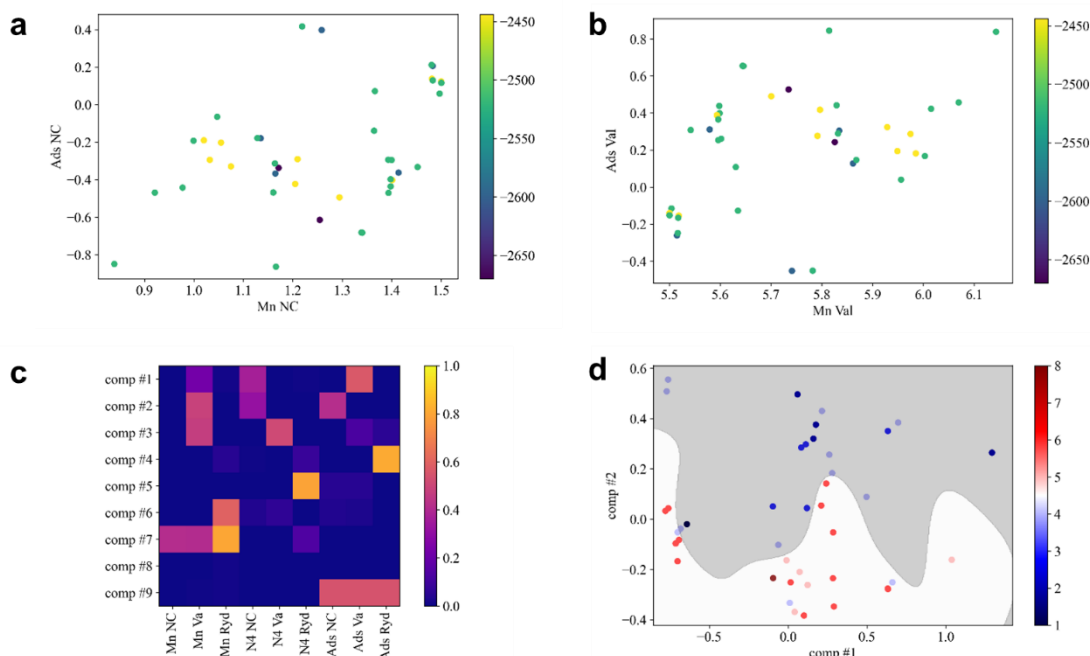


Figure 7 Collected data of energy as a function of (a) natural charge and (b) valence of Mn and adsorbates. (c) Normalized coefficient in PCA converting row-wise represented. (d) Classification of zones of low spin vs high spin based on PCA reduced first and second components.

In fact, such spin related energy shifts are broadly seen in many structures. Based on the calculation results of Mn single atom catalyst, we try to analyze from the perspective of natural population analysis (NPA), and explore the possible patterns of charge distribution, energy and spin. Based on all the calculated NPA results, the total Natural Charge (NC), Valence (Val) and Rydberg (Ryd) of Mn atom, N₄ structure and adsorbed groups have been selected, for a total of 9 sets of data. The number of valance electrons of the adsorbed groups is difficult to be compared horizontally because of the different groups, so the total number of valance electrons at

0 valence of each atom in the group is subtracted from this term. According to the generality of NPA, NC, Val and Ryd reflects the number of equivalent net charges of an atom in the system, the number of equivalent valence electrons an atom owns in the system and equivalent extra-valence shell of an atom because of the influence of other atoms in the system, respectively.

With the help of NPA dataset (see the Table below), one can sketch the energy distribution over various structures as a function of Mn NC and Ads NC (Figure 7a). Structures at different energies may have similar Mn NC and Ads NC, indicating that their electronic structures can show similar distribution despite different adsorbates. In addition, a similar conclusion can be given for valence electrons (Figure 7b). This phenomenon is positive evidence for the catalyst, because the unique electronic structure of the catalyst needs to be reflected in the adsorption, desorption and multiple intermediate steps/structures. Then there will be similar natural charge or valence electron distribution appearing in the structures of multiple intermediate steps.

Finally, based on NPA data, principle component analysis (PCA) were employed. At the data level, we did not perform normalization because the NPA results can be understood in terms of the number of charges, and normalization would destroy the charge number interpretation. The results showed that PCA could compress nine variables into two variables and still maintain an explained variance ratio of 97 percent. The principle components comp #1 and comp #2 transformed by PCA are shown in Figure 7c. comp #1 is mainly composed of Mn Val, Ads Val and N₄ NC, among which Ads Val is the most important. While comp #2 is mainly composed of Mn Val, Ads NC and N₄ NC, among which Mn Val is the most important. It can be seen that the first two variables of PCA describe the NPA of the electronic structure from the adsorbates and the metal Mn respectively, and the NC reflected by the N₄ structure is also very important, which needs to be described to a certain extent in order to comprehensively understand the change of the electronic structure in the catalytic processes. In addition, a support vector machine (SVM) classification model (Figure 7d) for spin described by comp #1 and comp #2 was established according to the composite indexes comp #1 and comp #2 transformed by PCA as descriptors. Rbf kernel (gamma=15) was adopted in the classifier and the regularization parameter is set to 10. And the regularization parameter is set to 10. If we call the spin below 4.5 a low spin state and above 4.5 a high spin state, depending on comp #1 and comp #2, the low and high spin states can be roughly separated by NPA results. The high spin states are mainly concentrated in the region where the sum of Mn Val, Ads NC and N₄ NC is negative. There are three expansions to high value comp #2 with different comp #1, and the whole classification boundary is w-shaped. This SVM classification roughly reflects the pattern of spin and charge/valence electron distribution.

5. Conclusions

In summary, we present a SAzyme with multi-enzyme mimicking activities by using amino-functionalized graphene quantum dots-derived Mn-N₄ single atom catalyst. Owing to the variation of spin states for Mn, the excellent SOD-like performance is demonstrated by experimental and theoretical results. We then systematically investigate catalytic mechanisms for POD-, CAT-, SOD-like activities via density functional theory (DFT) simulations, and it is disclosed that the excellent SOD-like activities can be attributed to its “spin flip-collection lock” in the “one-side adsorption” SOD-like catalytic process. Finally, spin related charge distributions on Mn-N₄ configurations by machine learning (ML) analysis suggest that the pattern of spin and natural charge/valence electron distribution will exhibit similarity in the structures of multiple intermediate steps of multi-enzyme mimicking activities.

This work links the spin with multi-enzyme mimicking activities of Mn-N₄ for the first time. We believe it will provide essential guidance for the future design and synthesis of highly active enzyme mimics and help understand the underlying catalytic mechanisms of nanozymes.

References

1. Chen, K. & Arnold, F. H. Engineering new catalytic activities in enzymes. *Nat Catal* **3**, 203–213

(2020).

2. Asakura, K., Nagahiro, H., Ichikuni, N. & Iwasawa, Y. Structure and catalytic combustion activity of atomically dispersed Pt species at MgO surface. *Applied Catalysis A: General* **188**, 313–324 (1999).
3. Gao, L. *et al.* Intrinsic peroxidase-like activity of ferromagnetic nanoparticles. *Nature Nanotech* **2**, 577–583 (2007).
4. Thomas, J. M., Raja, R. & Lewis, D. W. Single-Site Heterogeneous Catalysts. *Angew. Chem. Int. Ed.* **44**, 6456–6482 (2005).
5. Li, Z. *et al.* Iridium single-atom catalyst on nitrogen-doped carbon for formic acid oxidation synthesized using a general host–guest strategy. *Nat. Chem.* **12**, 764–772 (2020).
6. Liu, W. *et al.* Discriminating Catalytically Active FeN_x Species of Atomically Dispersed Fe–N–C Catalyst for Selective Oxidation of the C–H Bond. *J. Am. Chem. Soc.* **139**, 10790–10798 (2017).
7. Liu, X. *et al.* Constructing atomic Co1–N4 sites in 2D polymeric carbon nitride for boosting photocatalytic hydrogen harvesting under visible light. *International Journal of Hydrogen Energy* **47**, 12592–12604 (2022).
8. Ma, W. *et al.* A single-atom Fe–N₄ catalytic site mimicking bifunctional antioxidative enzymes for oxidative stress cytoprotection. *Chem. Commun.* **55**, 159–162 (2019).
9. Sahu, S. & Goldberg, D. P. Activation of Dioxygen by Iron and Manganese Complexes: A Heme and Nonheme Perspective. *J. Am. Chem. Soc.* **138**, 11410–11428 (2016).
10. Lyu, Z. *et al.* Single-Atom Nanozymes Linked Immunosorbent Assay for Sensitive Detection of A β 1–40: A Biomarker of Alzheimer’s Disease. *Research* **2020**, 2020/4724505 (2020).
11. Xu, B. *et al.* A Single-Atom Nanozyme for Wound Disinfection Applications. *Angew. Chem.* **131**, 4965–4970 (2019).
12. Huang, L., Chen, J., Gan, L., Wang, J. & Dong, S. Single-atom nanozymes. *Sci. Adv.* **5**, eaav5490 (2019).

13. Chen, F. *et al.* Molecular Engineering toward Pyrrolic N-Rich M-N₄ (M = Cr, Mn, Fe, Co, Cu) Single-Atom Sites for Enhanced Heterogeneous Fenton-Like Reaction. *Adv. Funct. Mater.* **31**, 2007877 (2021).
14. Zhang, S. *et al.* Single-atom nanozymes catalytically surpassing naturally occurring enzymes as sustained stitching for brain trauma. *Nat Commun* **13**, 4744 (2022).
15. Ji, S. *et al.* Matching the kinetics of natural enzymes with a single-atom iron nanozyme. *Nat Catal* **4**, 407–417 (2021).
16. Zhao, C. *et al.* Unraveling the enzyme-like activity of heterogeneous single atom catalyst. *Chem. Commun.* **55**, 2285–2288 (2019).
17. Jiao, L. *et al.* Densely Isolated FeN₄ Sites for Peroxidase Mimicking. *ACS Catal.* **10**, 6422–6429 (2020).
18. Huo, M., Wang, L., Wang, Y., Chen, Y. & Shi, J. Nanocatalytic Tumor Therapy by Single-Atom Catalysts. *ACS Nano* acsnano.9b00457 (2019) doi:10.1021/acsnano.9b00457.
19. Rulíšek, L., Jensen, K. P., Lundgren, K. & Ryde, U. The reaction mechanism of iron and manganese superoxide dismutases studied by theoretical calculations. *J. Comput. Chem.* **27**, 1398–1414 (2006).
20. Srnec, M., Aquilante, F., Ryde, U. & Rulíšek, L. Reaction Mechanism of Manganese Superoxide Dismutase Studied by Combined Quantum and Molecular Mechanical Calculations and Multiconfigurational Methods. *J. Phys. Chem. B* **113**, 6074–6086 (2009).
21. Kresse, G. & Furthmüller, J. Efficiency of ab-initio total energy calculations for metals and semiconductors using a plane-wave basis set. *Computational Materials Science* **6**, 15–50 (1996).
22. Kresse, G. & Furthmüller, J. Efficient iterative schemes for *ab initio* total-energy calculations using a plane-wave basis set. *Phys. Rev. B* **54**, 11169–11186 (1996).
23. Blöchl, P. E. Projector augmented-wave method. *Phys. Rev. B* **50**, 17953–17979 (1994).
24. Kresse, G. & Joubert, D. From ultrasoft pseudopotentials to the projector augmented-wave method. *Phys. Rev. B* **59**, 1758–1775 (1999).

25. Perdew, J. P., Burke, K. & Ernzerhof, M. Generalized Gradient Approximation Made Simple. *Phys. Rev. Lett.* **77**, 3865–3868 (1996).
26. Grimme, S., Antony, J., Ehrlich, S. & Krieg, H. A consistent and accurate *ab initio* parametrization of density functional dispersion correction (DFT-D) for the 94 elements H-Pu. *The Journal of Chemical Physics* **132**, 154104 (2010).
27. Grimme, S., Ehrlich, S. & Goerigk, L. Effect of the damping function in dispersion corrected density functional theory. *J. Comput. Chem.* **32**, 1456–1465 (2011).
28. Xia, C. *et al.* General synthesis of single-atom catalysts with high metal loading using graphene quantum dots. *Nat. Chem.* **13**, 887–894 (2021).
29. Pan, L. *et al.* Manipulating spin polarization of titanium dioxide for efficient photocatalysis. *Nat Commun* **11**, 418 (2020).
30. Deringer, V. L., Tchougréeff, A. L. & Dronskowski, R. Crystal Orbital Hamilton Population (COHP) Analysis As Projected from Plane-Wave Basis Sets. *J. Phys. Chem. A* **115**, 5461–5466 (2011).

Supplemental Information

In addition, the COHP curves of Mn-O bond in Figure S3c and S3d also elucidate the high barrier for the homolysis of H_2O_2^* to 2OH^* on the other side. It can be seen that the iCOHP is decreased from from -0.63 eV ($\text{Mn-N}_4\text{-H}_2\text{O}_2^*$) to -0.13 eV ($\text{Mn-N}_4\text{-OH}^*\text{-H}_2\text{O}_2^*$), so the weakened Mn-O interaction is also verified by a less negative iCOHP value of $\text{Mn-N}_4\text{-OH-H}_2\text{O}_2^*$ as well as the anti-bonding contributions of Mn-d and O-p orbitals overlap in the low-level electronic states (-6.2 eV). Therefore, the weakened Mn-O (oxygen atom in H_2O_2 molecule) interaction is account for the poor capacity of activating the second H_2O_2 molecule for Mn site on the other side. In addition, another probability of homolysis of H_2O_2^* catalytic path has also been proposed (Figure Sxa), the RDS is still the last desorption of H_2O molecule. Therefore, all the DFT simulated possible POD-like pathways suggest that the Mn-N_4 preferentially forms the Mn-O^* structure for the heterolysis of H_2O_2^* in a way of “bilateral adsorption” because of the more kinetically favorable reaction path.

On the other hand, the RDS in the “bilateral adsorption” catalytic mechanism is also investigated. For simplicity, we denote the four steps as follows: superoxide anion radical $\text{O}_2^{\cdot-}$ adsorption (step i), bilateral adsorptions (step ii), O_2 molecule release (step iii), H_2O_2 molecule generation and desorption (step iv). (i) The initialized state has an attached superoxide anion radical $\text{O}_2^{\cdot-}$ on the surface to form $\text{O}_2^{\cdot-*}$ (INT1 in Figure 5e) with no barriers, which is similar to that in “one-side adsorption”. (ii) Then, another superoxide anion radical $\text{O}_2^{\cdot-}$ can be adsorbed on the vacant side of the active site to form an $\text{O}_2^{\cdot-*} + \text{O}_2^{\cdot-*}$ intermediate state (INT2 in Figure 5e) with a favorable energy downhill of about -5 ~ -4 eV. (iii) After “bilateral adsorption” process, an O_2 molecule has been formed and the Mn-N_4 catalyst has stored extra electrons. As shown in Figure 5f and 5g, the iCOHP of Mn-O (oxygen atom in $\text{O}_2^{\cdot-*}$ and O_2^* , respectively) interaction is weakened from -1.53 eV ($\text{Mn-N}_4\text{-O}_2^{\cdot-*}$) to -0.05 eV ($\text{O}_2^{\cdot-*}\text{-Mn-N}_4\text{-O}_2^{\cdot-*}$). In addition, it can be seen from the DOS (Figure 5f and 5g) that d-p hybridization contributes less to bonding orbitals at deep levels for $\text{O}_2^{\cdot-*}\text{-Mn-N}_4\text{-O}_2^{\cdot-*}$. Therefore, the decreased Mn-O interaction is responsible for the converting from adsorbing $\text{O}_2^{\cdot-*}$ to desorbing O_2^* on oneside of the Mn-

N_4 surface due to the extra O_2^{*-} on the otherside. (iv) Subsequently, INT2 can react with a proton in the water to form $O_2^{*-}Mn-N_4-OOH^*$ where one electron lost and thus leads to a better desorption capacity of O_2 molecule on the other side. The generated $^{*-}Mn-N_4-OOH^*$ intermediate state (INT3 in Figure 5e) is still able to attract the second proton to generate H_2O_2 molecule (INT4 in Figure 5e). Finally, the simulations show that the desorption of H_2O_2 is the RDS with a moderate energy barrier of 0.539 eV, which is higher than that in “one-side adsorption”. Therefore, the simulation results suggest that the SOD-like process of $Mn-N_4$ exhibits an outstanding performance ($E_b = 0.077$ eV) in the “one-side adsorption” reaction pathway, even though the energy barrier is not high in “bilateral adsorption”.

For the spin state $S=0$, the energy is monotonically increasing, showing that O_2^- is sticking to the $Mn-N_4$ surface all the time. And for the spin state $S=1$, all the energetically favorable structures are found to have heavy spin contamination. Therefore, the rest two spin states ($S=2$ and 3) are taken into consideration.

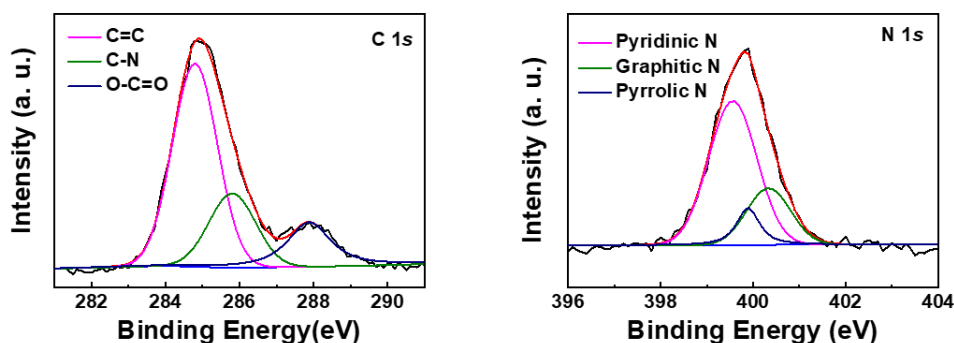


Figure S1 XPS spectra of Mn single-atom nanozymes in (a) C 1s and (b) N 1s regions.

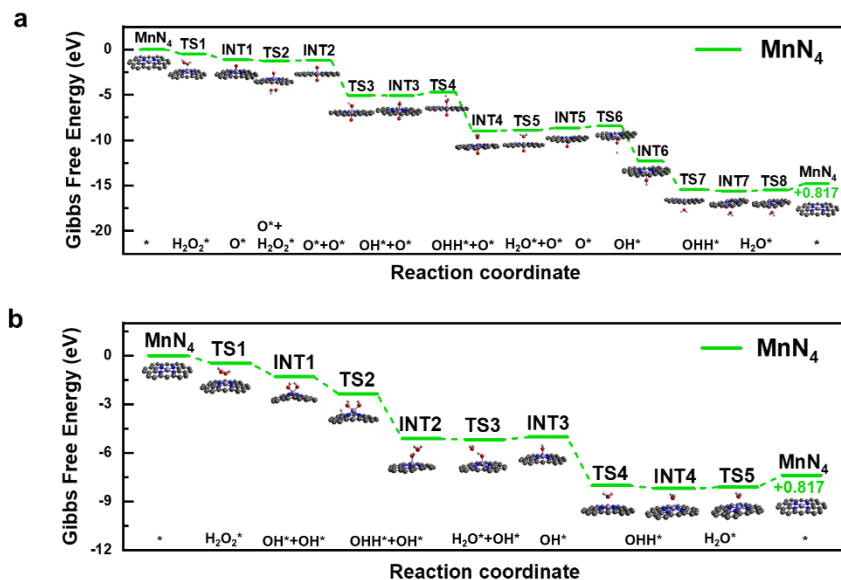


Figure S2 Calculated other possible reaction energy profiles corresponding to the peroxidase-like activity for (a) the heterolysis of $H_2O_2^*$ of MnN_4 corresponding to bilateral adsorption mechanism. (b) the homolysis of $H_2O_2^*$ of MnN_4 corresponding to one-side adsorption mechanism and The purple, blue, gray, red, and white balls represent the Mn, N, C, O, and H atoms, respectively.

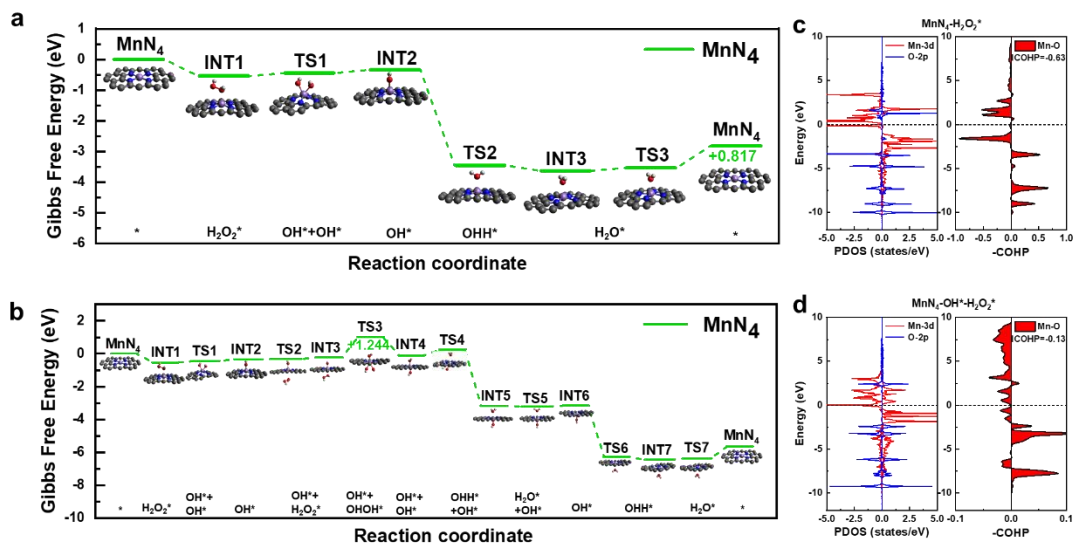


Figure S3 Calculated reaction energy profiles corresponding to the peroxidase-like activity for the homolysis of H_2O_2^* of MnN_4 corresponding to (a) one-side adsorption mechanism and (b) bilateral adsorption mechanism. The purple, blue, gray, red, and white balls represent the Mn, N, C, O, and H atoms, respectively. The DOS and COHP of (c) $\text{MnN}_4\text{-H}_2\text{O}_2^*$ and (d) $\text{MnN}_4\text{-OH-H}_2\text{O}_2^*$. All 2p orbitals indicate the 2p orbitals of one O atom in H_2O_2^* and all COHP is calculated for the Mn-O interaction, O indicates one of the oxygen atoms in H_2O_2^* .

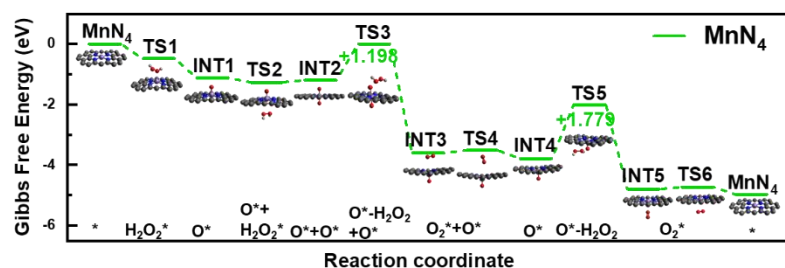


Figure S4 Calculated other possible reaction energy profiles corresponding to the catalase-like of MnN_4 corresponding to bilateral adsorption mechanism. The purple, blue, gray, red, and white balls represent the Mn, N, C, O, and H atoms, respectively.

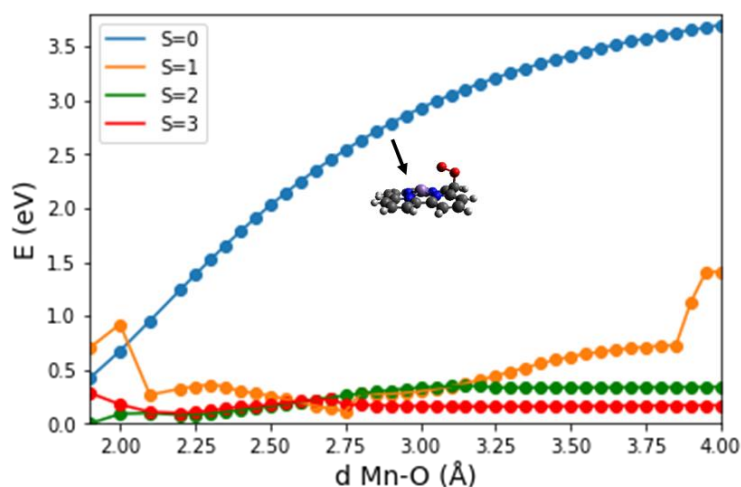


Figure S5 The energy profiles along with the Mn-O distances corresponding to the converting from superoxide anion radical O_2^* to O_2 molecule on the active site of MnN_4 at different spins.